Solar Energy Materials and Solar Cells 179 (2018) 372–379

Contents lists available at ScienceDirect

Solar Energy Materials and Solar Cells

journal homepage: www.elsevier.com/locate/solmat

# Broadband spectral response of diamond wire sawn mc-Si solar cell with omnidirectional performance and improved appearance

Y.F. Zhuang[a], S.H. Zhong[a], H.Y. Xu[a], W.Z. Shen[a,b,*]

[a] Institute of Solar Energy, and Key Laboratory of Artificial Structures and Quantum Control (Ministry of Education), Department of Physics and Astronomy, Shanghai Jiao Tong University, Shanghai 200240, People's Republic of China

[b] Collaborative Innovation Center of Advanced Microstructures, Nanjing 210093, People's Republic of China

ARTICLE INFO

*Keywords:*
Broadband spectral response
Omnidirectional
Solar cell
Diamond wire sawn
Multi-crystalline silicon

ABSTRACT

Highly efficient diamond wire sawn (DWS) multi-crystalline Si (mc-Si) solar cells with a satisfactory visual appearance are expecting to dominate the photovoltaic industry soon. Here, we report the realization of broadband spectral response of DWS mc-Si solar cells with omnidirectional performance and improved appearance. The success lies in the effective surface texturization based on MACE technique followed by post acid modification and the introduction of $SiO_2/SiN_x$ stack layers on the rear side. Bowl-like pits with an open size of about 1 μm are uniformly formed on the Si surface regardless of the crystallographic directions, which significantly enhances the antireflection ability in the short wavelength and makes the grain boundaries less noticeable. We have also shown that the bowl-like textured cells possess exceptional optical absorption over wide angles of incidence from 0° to 70°. Moreover, the $SiO_2/SiN_x$ stack layers enhance the rear internal reflection and passivation, effectively increasing the long wavelength absorption and suppressing the electrical losses. We have successfully mass-produced DWS mc-Si solar cells with an average efficiency of 19.1%, which is 1.2% absolutely higher than that of the conventional micro-textured counterparts.

## 1. Introduction

In recent years, multi-crystalline silicon (mc-Si) solar cell has occupied large percent of the photovoltaic industry market for its low cost. Nevertheless, the spectral responses in both short wavelength (< 600 nm) and long wavelength (> 900 nm) of industrial mc-Si solar cells are not sufficiently high, which are mainly attributed to the relatively high reflectance at the front surface and severe parasitic absorption as well as severe carrier recombination at Al rear reflector. This leads to a low conversion efficiency ($\eta$), especially for diamond wire sawn (DWS) mc-Si solar cells. The $\eta$ of conventional acid textured DWS mc-Si solar cells is about 0.4% absolutely lower than that of multi-wire slurry sawn ones [1], which sets significant barriers in promoting the industrialization of DWS mc-Si solar cells. Since DWS technique has several advantages including higher productivity, higher precision in cutting thin wafers and lower material waste [2–6], it is expected to occupy more than 50% in slicing mc-Si in the industry by 2020 [7]. Therefore, it is an urgent affair to realize high efficient DWS mc-Si solar cells with excellent spectral responses in both the short wavelength and long wavelength.

Many researches have demonstrated that Si nanostructures, such as nanowire arrays, have excellent broadband antireflection ability including in the short wavelength region [8–12]. However, the performances of such nanostructures based cells are not satisfactory due to the severe surface and Auger recombination that lead to strong electrical losses [13–15]. Recently, there are lots of reports demonstrating that metal-assisted chemical etching (MACE) technique combined with post alkaline modification is effective to overcome these disadvantages [1,16,17]. By employing this method, we have fabricated micro/nano composite structures with satisfactory antireflection properties and acceptable electrical losses, and an absolute increase of 0.57% in $\eta$ was achieved on DWS mc-Si solar cells [18]. Nevertheless, owing to the anisotropic etching property of alkaline solution, different micro- or nano-structures are formed on different crystallographic planes, leading to the unsatisfactory appearance of DWS mc-Si solar cells. Therefore, it is urgent to develop a surface texture that can effectively improve short wavelength spectral responses with an acceptable appearance for DWS mc-Si solar cells.

In addition, it is also necessary to further improve the optical and electrical properties in the long wavelength range by rational design of cell structures. Through introducing dielectric thin films ($SiO_2$, $SiN_x$, or $SiO_2/SiN_x$ stack layers) at the rear surface, Holman et al. [19]

* Corresponding author at: Institute of Solar Energy, and Key Laboratory of Artificial Structures and Quantum Control (Ministry of Education), Department of Physics and Astronomy, Shanghai Jiao Tong University, Shanghai 200240, People's Republic of China.

*E-mail address:* wzshen@sjtu.edu.cn (W.Z. Shen).

https://doi.org/10.1016/j.solmat.2017.12.039
Received 8 May 2017; Received in revised form 18 December 2017; Accepted 22 December 2017
Available online 29 December 2017
0927-0248/ 

demonstrated that parasitic absorption in the Al rear reflector in the long wavelength range can be effectively suppressed when the thickness of the dielectric film is more than 100 nm, resulting in enhanced spectral response in the long wavelength and cell performances. Moreover, these dielectric films can effectively passivate the rear surface, reducing the photogenerated carrier loss at the rear surface [20]. These advantages have been verified in our 20% efficient nanostructures textured single-crystalline Si solar cells [21] and the industrial single-crystalline Si solar cells with a high $\eta$ of 22.13% [22].

In this study, by employing MACE technique with post acid modification, and the introduction of $SiO_2/SiN_x$ stack layers at the rear surface, we have successfully fabricated bowl-like structures textured DWS mc-Si solar cells with an improved visual appearance and a high $\eta$ of 19.1% with a large wafer size of 156 × 156 mm$^2$. The achieved $\eta$ of our samples is 1.2% absolutely higher than that of the conventional micro-texture (CM-T) based counterparts. In addition, our cells possess excellent broadband spectral response due to the outstanding antireflection performance in short wavelength and suppressed parasitic absorption in long wavelength together with reduced carrier recombination at the rear surface. Furthermore, the cells also possess exceptional optical absorption over wide angles of incidence (AOI) from 0° to 70°, exhibiting omnidirectional property, which is beneficial to the electric power generation since the AOI changes with the rotation of the earth. We believe that DWS mc-Si solar cells with appropriate surface texture and rational rear design will soon become the mainstream in the mc-Si solar cell industry.

## 2. Experimental

### 2.1. Texturization and fabrication of the DWS mc-Si solar cells

In this work, the used Si wafers were p-type DWS mc-Si with a size of 156 × 156 mm$^2$, a thickness of 200 ± 20 µm and resistivity of 1–3 Ω cm. The texturization and cell fabrication processes are shown in Fig. 1. Deionized water (DIW) cleaning was performed after every step. Firstly, saw damage etching was employed by acid solution. After that, the wafers were immersed into MACE solution (2.4 M HF/1.7 M $H_2O_2$/0.0002 M $AgNO_3$) for 4 mins at 50 °C. In this process, Ag nanoparticles were deposited onto the Si substrate and nano-pores were formed. Then the nano-pores were enlarged by immersing the wafers into the mixed solution of HF:$HNO_3$:DIW = 1:6:3 (volume ratio) for different modification times of 30 s, 50 s, 100 s (labeled as $T_{30}$, $T_{50}$, and $T_{100}$), respectively, at the temperature of 8 °C. Finally, all the textured wafers were immersed in the solution of $HNO_3$:DIW = 1:1 (volume ration) for 8 mins to remove the residual metal impurities, followed by rinsing with DIW and spin-drying. In addition, CM-T samples were prepared as the reference by dipping the wafers into the mixed HF/$HNO_3$/DIW (1:5:4) solution for 3 mins at 8 °C.

After the texturization and industrial cleaning processes, one group of the wafers underwent a standard industrial solar cell fabrication process, including n-type diffusion on one side with $POCl_3$ as diffusion source (M5111-4WL/UM, CETC 48th Research Institute), removal of the phosphorous silicate glass (PSG) in dilute HF solutions, deposition of $SiO_2/SiN_x$ layers on the front surface by plasma enhanced chemical vapor deposition (PECVD) system (M82200-6/UM, CETC 48th Research Institute), the fabrication of front and back electrodes by screen printing technique (PV1200, DEK) and co-firing process (CF-Series, Despatch).

Another group of the wafers underwent a distinct cell fabrication process. Firstly, the rear surface was polished by NaOH/$H_2O_2$ solution. Then the $SiO_2/SiN_x$ stack layers were deposited on the rear side by PECVD at 450 °C for 40–100 mins. Subsequently, n$^+$-emitter was formed on the front side during the diffusion process for about 100 mins at 800 °C. After the PSG removing process, local line openings were formed on the rear $SiO_2/SiN_x$ stack layers by laser ablating (DR-LA-Y40, DR Laser), followed by an annealing process at 700 °C for 60 mins. After that, $SiO_2/SiN_x$ stack layers were deposited on the front side by PECVD for about 40 mins at 400 °C. Finally, the wafers underwent the same screen printing and the co-firing processes as mentioned above. The diagram of the cell structure is illustrated in the middle part of Fig. 1.

### 2.2. Fabrication of the samples for recombination comparison

For the study of effective minority carrier lifetime ($\tau_{eff}$), $SiO_2/SiN_x$ stack layers were symmetrically deposited on both sides of the polished wafers by PECVD at 450 °C for 100 mins and followed by an annealing process at 550 °C to 850 °C for 60 mins.

### 2.3. Characterization

The morphologies of the wafers were investigated by field emission scanning electron microscopy (Zeiss Ultra Plus). The reflectance spectra and external quantum efficiency (EQE) were measured by QEX10 (PV MEASUREMENTS). Minority carrier lifetime measurements were carried out by quasi-steady state photoconductance decay method in Semilab WT1200 equipment. And the electrical parameters of the solar cells were measured under AM1.5 spectrum at the temperature of 25 °C.

### 2.4. Simulations of reflectance

The surface reflectance of CM-T over the AOIs from 0° to 80° was simulated by setting the periodic grooves with 2 µm in width and 400 nm in height on the surface of 180 µm Si substrate by online wafer ray tracer provided by PV light house, which is a professional optical simulator for the Si microstructures-textured solar cells. AM1.5 spectrum was used in our cases and the max total rays were set to 50,000 to enhance the accuracy. The surface reflectance of our bowl-like structures was numerically calculated by Lumerical finite difference time

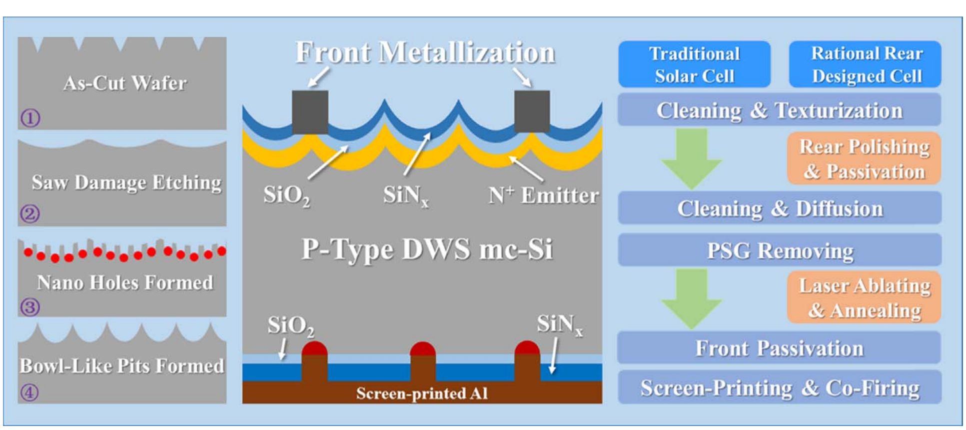


**Fig. 1.** Schematic illustration of the main steps for texturization (left) and fabrication (right) of the DWS mc-Si solar cells, together with the diagram of the cell structure (middle).

domain software. Periodic bowl-like structures with the open size of 1 μm and the depth of 600 nm was located at the surface of Si substrate on x-y plane, and 1.5 μm in the z-direction. Bloch boundary in the x-y region was adopted because oblique incidence with the AOIs from 0° to 80° was employed in our cases. But the boundary in the z-directions was perfectly matched layers and hence the thickness of the substrate was equivalent to infinitely thick. Note that the polarization AOI was set to be 45°, which will lead to the simulated results the same with averaging those of P-polarization and S-polarization.

### *2.5. Simulations of optical absorption in Al rear reflector*

The simulations of optical absorption in Al rear reflector were carried out by the online wafer ray tracer. $SiO_2/SiN_x$ stack layers were set on both surfaces of the Si substrate. The thickness of the stack layers at the front surface was 80 nm while it varied 0–450 nm at the rear surface. Pure Al layer was treated as the Al rear reflector in our cases, and the thickness of Al layer was 3 μm, which guaranteed that no light can transmit through it.

## 3. Result and discussion

### *3.1. Modified surface morphology by combining MACE with post acid etching*

Fig. 2a shows the SEM image of the CM-T samples. Parallel grooves with different widths (from nanometers to micrometers) are closely formed on the Si surface. Such structures are, however, not suitable for solar cells due to the high reflectance and unsatisfactory cell appearance. In order to realize effective textures on DWS mc-Si wafers, systematic investigation was conducted in this work. Firstly, the wafers underwent a pretreatment process to eliminate the saw damage layer and achieve a better surface condition. After that, MACE technique is employed. During the MACE process, Ag nanoparticles are firstly deposited onto the surface of Si substrate based on the galvanic displacement reaction. Since the equilibrium potential of $Ag^+/Ag$ couple ($E^\circ = 0.8$ V) is more positive than the valence band energy of Si ($E_{VB} = 0.67$ V) [23], $Ag^+$ ions capture electrons from the valance band of Si, leading to the oxidization of Si atoms. Then the Si oxide under the Ag particles is removed by HF immediately. As a consequence, Ag nanoparticles help to form pits on Si substrate and embed themselves in the pits. Meanwhile, the Si substrate is also corroded by $HF/H_2O_2$. Based on the experiment results presented in the literature [23–25], the oxide formation and dissolution rates of Si are much higher at the Ag/Si interface than the one at Ag free regions owing to the catalytic activity of Ag nanoparticles. Accordingly, deep pores are formed with increasing etching time and the Ag particles sink at the bottom of pores. Although such structures solely fabricated by the MACE method are effective to reduce surface reflectance, they are not suitable for solar cells due to the large surface area, which leads to a severe surface recombination [15]. Therefore, further surface modification is necessary by post etching processes. In our study, the surface structures are finally modified by $HF/HNO_3$ etching to reduce the surface area and form a better texture.

Fig. 2b–d illustrate the SEM images of $T_{30}$, $T_{50}$ and $T_{100}$ samples, respectively, which confirmed that the saw marks are perfectly removed. For the case of $T_{30}$, the wafer exhibits a rough surface and cylindrical pores with the open size of about 500 nm are obtained. With increasing etching time, the pores are expanded and connected to their neighbors, resulting in that bowl-like pits with the open size of about 1 μm are randomly formed on the whole surface, as shown in Fig. 2c. Note that the surface becomes smoother with the enlargement of the pits. By further extending the etching time, the pits further merge to others and become larger pits, e.g., when the etching time is increased to 100 s, the open sizes of the pits are about 2 μm in diameter (Fig. 2d). In general, the open size of the structures can be controlled accurately from nanoscale to microscale by increasing the etching time.

There are many researches showing that Si nanostructures fabricated by MACE combined with post alkaline etching is effective to improve the performances of DWS mc-Si solar cells [1,16–18]. However, owing to the anisotropic etching of the alkaline solution, different structures are formed on different crystallographic planes of mc-Si, which leads to the non-uniform reflectance of the surface, as well as the non-uniform thickness of the coated antireflection layer. As a result, unsatisfactory visual appearance of the cells with mixed light blue regions and dark blue regions is observed [18]. In contrast, acid etching

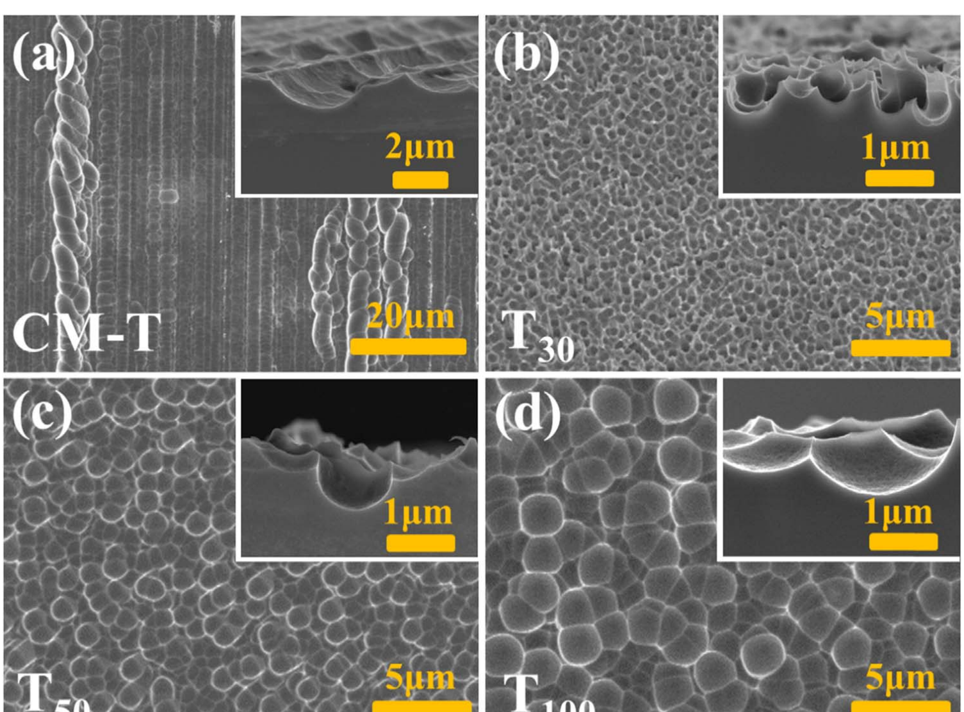


**Fig. 2.** SEM images of (a) conventional micro-texture (CM-T) and the textured wafers based on MACE technique followed by acid modification for (b) 30 s ($T_{30}$), (c) 50 s ($T_{50}$), (d) 100 s ($T_{100}$), together with the cross-section view shown in the inset.

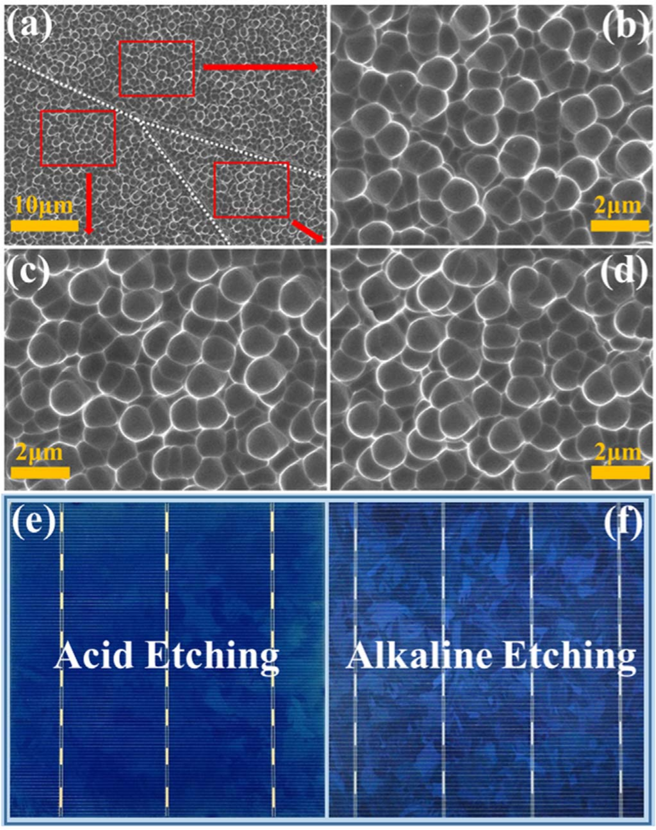


**Fig. 3.** SEM images of: (a) $T_{50}$ surface on different crystalline grains and (b)-(d) zoomed-in figures of the red frame zones in (a), together with digital photography of DWS mc-Si solar cells textured by MACE technique followed by (e) acid modification in this work and (f) alkaline modification. (For interpretation of the references to color in this figure legend, the reader is referred to the web version of this article.)

does not depend on crystallographic directions so that isotropic etching of Si happens, and hence it is more suitable for texturing mc-Si substrate [26]. In our cases, all the texturization processes are under acidic conditions, exhibiting a great potential to form uniform textures on mc-Si surface. As an example, Fig. 3a presents the SEM images of the $T_{50}$ surface on different crystalline grains. The white dash lines guide the grain boundaries. The zoomed-in figures of the red frame zones are shown in Fig. 3b–d. We can see that similar structures are formed on different crystallographic planes of Si, which is attributed to isotropic etching of Si. Fig. 3e–f present the photos of the acid-textured cell in this work and an MACE textured with post alkaline modified cell, respectively. Obviously, the acid-textured cell exhibits a better appearance with less noticeable grain boundaries, compared with that of alkaline-modified cell.

### 3.2. Optical characteristics and electrical analysis

In order to find the appropriate texture for DWS mc-Si solar cells, we investigate the influence of the surface structures on both optical and electrical properties. Fig. 4a illustrates the reflectance spectra of the textured wafers and cells in the wavelength ranging from 400 nm to 1100 nm, together with the averaged reflectance ($R_{ave}$) in the inset. Note that $R_{ave}$ is calculated by averaging the reflectance over the standard AM1.5 spectrum in the wavelength ranging from 400 nm to 1100 nm as follows:

$$R_{ave} = \frac{\int_{400\,\text{nm}}^{1100\,\text{nm}} R(\lambda)\cdot S(\lambda)\cdot \mathrm{d}\lambda}{\int_{400\,\text{nm}}^{1100\,\text{nm}} S(\lambda)\cdot \mathrm{d}\lambda} \tag{1}$$

where $R(\lambda)$ represents the experimental reflectance and $S(\lambda)$ represents the standard AM1.5 solar photon spectral distribution. It is obvious that the reflectance of $T_{30}$ and $T_{50}$ are much lower than that of CM-T and $T_{100}$. Especially, $T_{30}$ exhibits the lowest reflectance with an average value of about 14.5%. With increasing the etching time in $HF/HNO_3$, the reflectance of the resultant structures increases gradually and a high $R_{ave}$ of 26.5% is reached for $T_{100}$. For solar cells with $SiO_2/SiN_x$ stack layers, antireflection effect is enhanced in the whole wavelength range. However, for the CM-T and $T_{100}$ cases, the reflectance is still very high in the short wavelength region (< 650 nm) with the highest value of over 35%, leading to a high $R_{ave}$ of 11.5% and 9.2%, respectively. In contrast, $T_{30}$ and $T_{50}$ present low reflectance in the whole wavelength ranging from 500 to 1000 nm and the $R_{ave}$ is about 6%.

Fig. 4b exhibits the measured EQE data of the cells. As expected, the EQE of $T_{50}$ cells is much higher at short wavelength compared with that of CM-T and $T_{100}$ cells, which is attributed to the enhanced antireflection ability of the surface texture in the short wavelength range. Nevertheless, $T_{30}$ cells have much lower EQE in the whole wavelength range despite of their lowest reflectance. It is well known that Si nanostructures usually have a large surface area and nanostructures with very small open size are difficult to be passivated, leading to much severer surface and near surface recombination. As a consequence, severe degradation of the EQE occurs. Generally, in order to achieve high performances of solar cells, there is a tradeoff between optical gain and electrical losses. In our cases, surface texture with $T_{50}$ is the appropriate choice for high performance solar cells.

### 3.3. Omnidirectional characteristics of the DWS mc-Si cells

As presented above, $T_{50}$ cells exhibit the best performances when measured under normal incidence. It is also highly necessary to understand the cell performances over different AOIs, since in the real application the AOI changes with the rotation of the earth. We illustrate in Fig. 5a–b the measured EQEs of the CM-T and $T_{50}$ cells over the AOIs ranging from 0° to 80°, respectively. When the AOI is less than 60°, the EQE spectra of the CM-T cells are almost overlapped. When the AOI is increasing to 70°, a slight drop of EQE occurs, while it drops rapidly over the AOIs more than 70°. Interestingly, for the $T_{50}$ cells, similar trend is observed. Namely, both the CM-T and $T_{50}$ cells exhibit excellently broad-angle EQE spectra, which is beneficial for solar cell application. Nevertheless, it should be pointed out that $T_{50}$ cells exhibit higher EQE properties in the short wavelength range for all AOIs, compared with CM-T counterparts. Fig. 5c presents the calculated short-circuit current density ($J_{SC}$) of CM-T and $T_{50}$ cells over the AOIs ranging from 0° to 80° according to the EQE spectra shown in Fig. 5a–b. The $J_{SC}$ is calculated by:

$$J_{SC} = q\int_{400\,\text{nm}}^{1100\,\text{nm}} EQE(\lambda)\cdot S(\lambda)\cdot \mathrm{d}\lambda \tag{2}$$

where $q$ denotes electron charge. To make the variation trend clearer, AM1.5 solar photon spectral distribution is assumed for all cases. For CM-T cells, when the AOI is less than 70°, the $J_{SC}$ remains at about 35 mA/cm$^2$, while it drops to about 26 mA/cm$^2$ at the AOI of 80°. For $T_{50}$ cells, the $J_{SC}$ remains at a high level of over 36 mA/cm$^2$ over the AOIs from 0° to 70°, while it drops to about 30 mA/cm$^2$ at the AOI of 80°. The results show that $T_{50}$ cells exhibit higher $J_{SC}$ over all AOIs compared with CM-T counterparts, which is beneficial for higher electric power generation in a day or a year.

To get insight into the above observation, simulation of the reflectance varying with AOIs and wavelengths was implemented. As shown in Fig. 5d, the reflectance behaviors varying with AOIs are similar for both CM-T and $T_{50}$ cases at the wavelength of 600 nm, 800 nm and 1000 nm. When the AOI is less than 70°, the reflectance is not sensitive to the increase of AOI, but it increases rapidly when the AOI is over 70°, and reaches a high level of over 40% at the AOI of 80°. These results demonstrate that both the CM-T and $T_{50}$ exhibit omnidirectional antireflection properties over broad AOIs from 0° to 70°. However, the

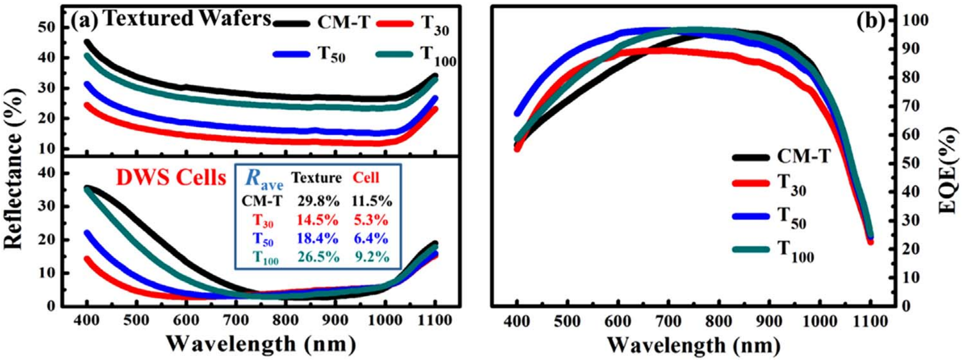


**Fig. 4.** (a) Reflectance spectra (400–1100 nm) of the textured wafers and fabricated cells, together with the averaged reflectance ($R_{ave}$) of the reflectance spectra in the inset. (b) Experimental EQE of the fabricated DWS mc-Si solar cells.

reflectance of $T_{50}$ is much lower than that of CM-T over all AOIs and all wavelengths, which is attributed to the superior antireflection ability of the modified surface texture. Obviously, the antireflection behaviors can well explain the EQE or $J_{SC}$ observation as a function of AOI in Fig. 5a–c.

### 3.4. Rational design of the rear surface

Based on the results presented above, we have successfully improved the spectral response of the cells in the short wavelength range and the omnidirectional optical absorption by the modified bowl-like texture. However, to realize highly efficient DWS mc-Si solar cells, it is also very important to improve the cell properties in the long wavelength range by the rational design of the rear surface. We have previously demonstrated that rear side passivation by $SiO_2/SiN_x$ stack layers can effectively increase the long wavelength responses of the cells [21]. However, the mechanisms behind it are not fundamentally clear enough and need to be further studied.

Fig. 6a illustrates the reflectance in long wavelength of the cells with $SiO_2/SiN_x$ layers deposited on the rear side. The thickness of the deposited stack layers is 0 nm, 100 nm, 250 nm, 350 nm, respectively (the inner $SiO_2$ is about 25 nm thick). When there are no $SiO_2/SiN_x$ layers on the rear side, the cells exhibit low reflectance in long wavelength, i.e., about 20% at 1200 nm. When the thickness of the $SiO_2/SiN_x$ layers are 100 nm, the long wavelength reflectance is drastically increased and reaches about 40% at 1200 nm. With further increasing $SiO_2/SiN_x$ thickness, the long wavelength reflectance continues to increase and finally reaches the maximum (about 45% at 1200 nm) for the stack layers thicknesses of more than 250 nm (the reflectance spectra of 250 nm and 350 nm cases are almost overlapped). Note that the increase of reflectance in the long wavelength here indicates more light reflect back from rear surface and thus more light will be re-absorbed in the Si substrate [21].

To further reveal the mechanism behind the increased reflectance in long wavelength, we have carried out the simulation of the optical absorption in Al rear reflector varying with the thickness of rear $SiO_2/SiN_x$ layers from 0 to 450 nm, as shown in Fig. 6b. When there are no $SiO_2/SiN_x$ layers on the rear side, high optical absorption in Al rear reflector is observed. With increasing the thickness of the $SiO_2/SiN_x$ layers, the absorption decreases dramatically and reaches the minimum for $SiO_2/SiN_x$ thickness of more than 250 nm, which is owing to less penetration of evanescent waves and hence the diminishing parasitic absorption in Al rear reflector [27]. As a result, more light in long wavelength can reflect back into the Si substrate, which is well agreement with the reflectance observation shown in Fig. 6a.

Besides the increased optical absorption in Si substrate, $SiO_2/SiN_x$

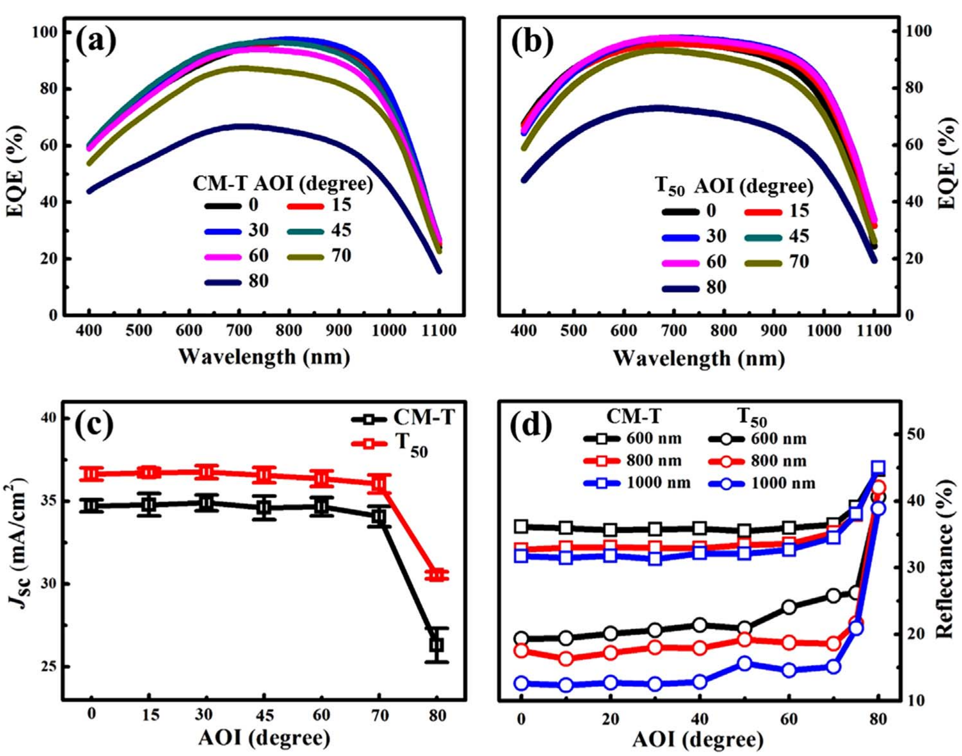


**Fig. 5.** Experimental EQE spectra of the (a) CM-T and (b) $T_{50}$ solar cells varying with AOIs, together with (c) comparison of their calculated $J_{SC}$ versus AOIs according to the EQE spectra. (d) Simulation of the reflectance of CM-T and $T_{50}$ varying with AOIs at 600 nm, 800 nm and 1000 nm.

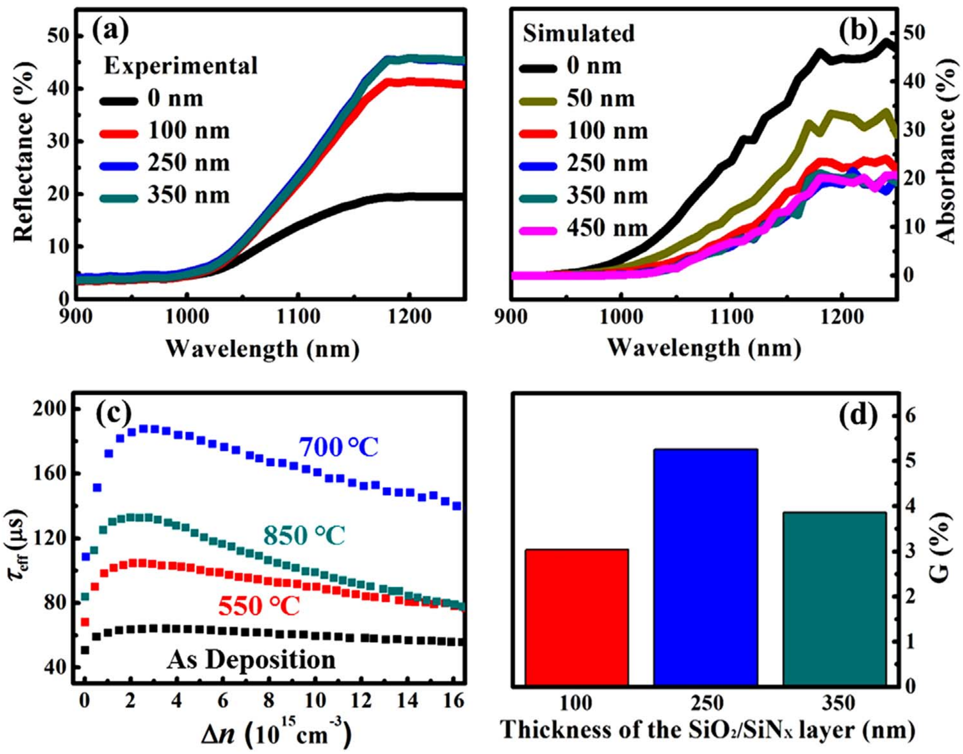


**Fig. 6.** (a) Experimental reflectance spectra of the DWS cells with $SiO_2/SiN_x$ stack layers deposited on the rear side. (b) Simulated optical absorption in the Al rear reflector with $SiO_2/SiN_x$ stack layers deposited on the rear side. (c) $\tau_{eff}$ with respect to the injection level $\Delta n$ at different annealing temperatures. (d) Comparison of enhancement factor G of $\eta$ of the cells with different thicknesses of rear $SiO_2/SiN_x$ stack layers.

stack layers with a post annealing process can also effectively passivate the Si surface to suppress the electrical losses of the cells. Fig. 6c illustrates the influence of the different annealing temperatures on the effective minority carrier lifetime $\tau_{eff}$ with respect to the injection level ($\Delta n$). $SiO_2/SiN_x$ stack layers were deposited on both sides of the polished Si substrate and the annealing process was performed in the air atmosphere for 60 mins at 550 °C, 700 °C and 800 °C, respectively. Obviously, the $\tau_{eff}$ values of the annealed samples are much higher than those of the as-deposited ones, and the highest $\tau_{eff}$ is achieved at the optimized annealing temperature of 700 °C, e.g., at $\Delta n = 1\times 10^{15}\,cm^{-3}$, it is about 170 μs. According to the $\tau_{eff}$, surface recombination velocity ($S_{eff}$) can be determined by the following equation [28]:

$$\frac{1}{\tau_{eff}} = \frac{1}{\tau_{bulk}} + \frac{2S_{eff}}{W} \tag{3}$$

where $\tau_{bulk}$ presents the bulk recombination lifetime and $W$ presents the wafer thickness (≈ 180 μm). Here, we only consider the intrinsic $\tau_{bulk}$ according to the formula by Richter et al. [29] and thus the calculated $S_{eff}$ represents the upper limit of the surface recombination velocity. The calculated $S_{eff}$ of 5.9 cm/s demonstrates an excellent passivation effect of $SiO_2/SiN_x$ stack layers for a solar grade p-type Si wafer.

Finally, in order to evaluate the comprehensive influence of the rear $SiO_2/SiN_x$ stack layers on the cell performance, we define the enhancement factor (G) of the $\eta$ of the rear $SiO_2/SiN_x$ deposited cells relative to that ($\eta_0$) of the conventional cells without rear $SiO_2/SiN_x$ stack layers:

$$G = \frac{\eta - \eta_0}{\eta_0} \tag{4}$$

As shown in Fig. 6d, the results show that 250 nm is the appropriate thickness for the rear $SiO_2/SiN_x$ stack layers in our cases, and the highest G of about 5.2% is achieved. Note that thicker $SiO_2/SiN_x$ stack layers may lead to higher series resistance ($R_S$) and lower fill factor (*FF*), which affects the $\eta$ of the cells.

### *3.5. Broadband spectral response of DWS mc-Si solar cells*

We have mass-produced the DWS mc-Si solar cells ($T_{50\text{-}Broad}$) based on the simultaneous adoption of the $T_{50}$ texture at the front surface and the $SiO_2/SiN_x$ stack layers at the rear surface. To demonstrate the broadband spectral response advantage of such solar cell design, we compare the EQE spectra and current-voltage (*I-V*) parameters of the $T_{50\text{-}Broad}$ cells with those of CM-T counterparts. As shown in Fig. 7a, in the short wavelength range, the EQE of $T_{50\text{-}Broad}$ cells is much higher, which is attributed to the outstanding antireflection ability of the bowl-like structures. In the long wavelength range, the $T_{50\text{-}Broad}$ cells also exhibit higher EQE owing to the suppressed penetration of evanescent waves and excellent surface passivation effect by $SiO_2/SiN_x$ stack layers. As the overall result, the $T_{50\text{-}Broad}$ cells present higher EQE almost over the whole wavelength range, demonstrating the significance of optimizing the front surface texture and rear cell structure on the cell performances. Fig. 7b shows the measured *I-V* parameters including open circuit voltage ($V_{OC}$), short circuit current ($I_{SC}$), *FF* and $\eta$ of the CM-T and $T_{50\text{-}Broad}$ DWS mc-Si solar cells. Compared with CM-T cells, the average $V_{OC}$ of $T_{50\text{-}Broad}$ cells is much higher with an absolute increment value of 9 mV, reaching 639 mV, which suggests that the passivation for the both sides of the Si substrate by $SiO_2$ /$SiN_x$ stack layers effectively suppresses the electrical losses. In addition, owing to the enhanced spectral response in both the short wavelength and long wavelength, high $I_{SC}$ with the average value of 9.32 A is achieved for $T_{50\text{-}Broad}$ cells, which is 0.59 A absolutely higher than that of CM-T counterparts. Resulting from the high performance of $V_{OC}$ and $I_{SC}$, we have successfully mass-produced DWS mc-Si solar cells with an average $\eta$ of 19.1%. Compared with the CM-T cells, absolute increment of about 1.2% of $\eta$ is achieved (see the distribution ration in Fig. 7b). Fig. 7c presents the *I-V* characteristics of the best CM-T and $T_{50\text{-}Broad}$ solar cells. The highest $\eta$ of our $T_{50\text{-}Broad}$ cells reaches 19.3% and the maximum output power is 4.7 W on the wafer size of 243.36 $cm^2$, which is 0.3 W absolutely higher than that of CM-T counterparts. Generally, the cell performance can be further improved by optimizing the cell fabrication processes. Our results present the potential to realize high efficient DWS mc-Si solar cells in mass production by employing our surface texture

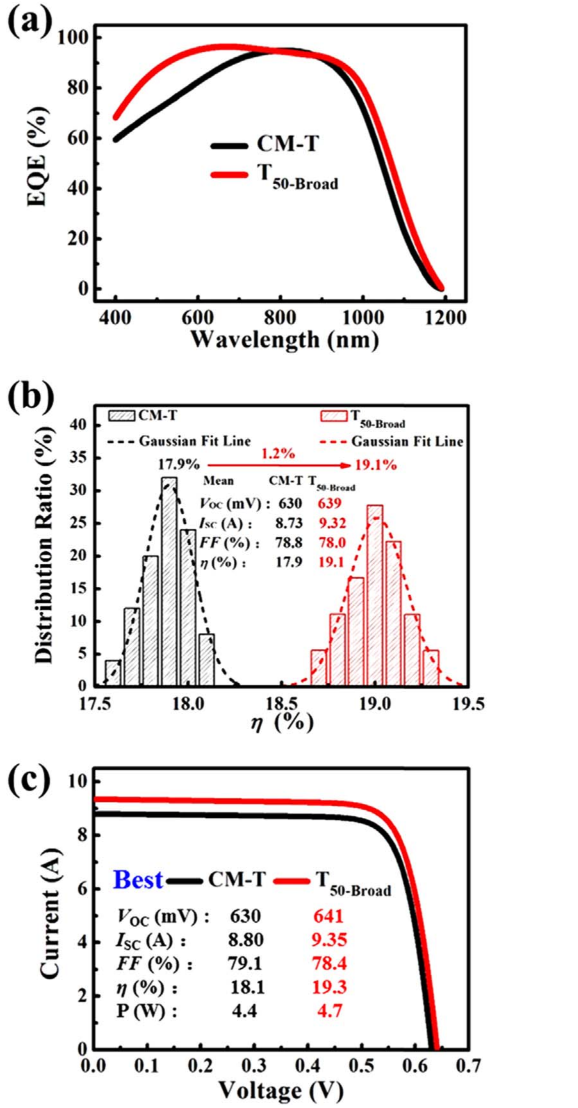


**Fig. 7.** Comparison of (a) the EQE spectra, (b) the measured *I-V* parameters including $V_{OC}$, $I_{SC}$, *FF* and $\eta$, and (c) *I-V* characteristics of the CM-T and $T_{50\text{-Broad}}$ DWS mc-Si solar cells.

method and rear cell design.

## 4. Conclusions

In summary, we have successfully fabricated high-efficiency DWS mc-Si solar cells on the standard wafer size of 156 × 156 $mm^2$. On the one hand, by employing MACE technique together with post acid modification, bowl-like structures are uniformly formed on the whole surface of the Si substrate regardless of the crystallographic directions, which makes the grain boundaries less noticeable and guarantees an improved visual appearance of the cells compared to those of the CM-T based cells and MACE textured with post alkaline modification cells. The bowl-like structures with the open size of about 1 μm also exhibits outstanding antireflection ability in the short wavelength and the omnidirectional antireflection characteristics. We have further demonstrated that the bowl-like structures textured cells possess exceptional optical absorption over wide AOIs from 0° to 70°, which is beneficial to the electric power generation in the real application. On the other hand, we have introduced the $SiO_2/SiN_x$ stack layers at the rear surface to effectively suppress the penetration of evanescent waves in Al rear reflector in the long wavelength, and hence more light can reflect back into the Si substrate and be re-absorbed. The $SiO_2/SiN_x$ stack layers can also effectively passivate the Si surface after annealing process to suppress the electrical losses of the cells. Based on the simultaneous adoption of the bowl-like texture at the front surface and the $SiO_2/SiN_x$ stack layers at the rear surface, our DWS mc-Si solar cells possess excellent broadband spectral response with an average $\eta$ of 19.1%, which is 1.2% absolutely higher than that of the CM-T counterparts. We believe that the front surface texture method and the rear cell design presented in the study will contribute to the mass-production of DWS mc-Si solar cells with high efficiency.

## Acknowledgements

This work was supported by the National Natural Science Foundation of China (61234005, 11474201 and 11674225), and China Postdoctoral Science Foundation (15Z102060052 and 16Z102060054).

## References

[1] F. Cao, K.X. Chen, J.J. Zhao, X.Y. Ye, J.J. Li, S. Zou, X.D. Su, Next-generation multicrystalline silicon solar cells: diamond-wire sawing, nano-texture and high efficiency, Sol. Energy Mater. Sol. Cells 141 (2015) 132.
[2] N. Watanabe, Y. Kondo, D. Ide, T. Matsuki, H. Takato, I. Sakata, Characterization of polycrystalline silicon wafers for solar cells sliced with novel fixed-abrasive wire, Prog. Photovolt. Res. Appl. 18 (2010) 485.
[3] B. Meinel, T. Koschwitz, J. Acker, Textural development of SiC and diamond wire sawed scsilicon wafer, Energy Procedia 27 (2012) 330.
[4] W.I. Clark, A.J. Shih, C.W. Hardin, R.L. Lemaster, S.B. McSpadden, Fixed abrasive diamond wire machining-part I: process monitoring and wire tension force, Int. J. Mach. Tool Manuf. 43 (2003) 523.
[5] A. Bidiville, K. Wasmer, R. Kraft, C. Ballif, Diamond wire-sawn silicon wafers- from the lab to the cell production, in: Proceedings 24th EU PV-SEC, 2009.
[6] X.G. Yu, P. Wang, X.Q. Li, D.R. Yang, Thin Czochralski silicon solar cells based on diamond wire sawing technology, Sol. Energy Mater. Sol. Cells 98 (2012) 337.
[7] Photovoltaic Roadmap 2016, China Photovoltaic Industry Association (CPIA).
[8] E. Garnett, P. Yang, Light trapping in silicon nanowire solar cells, Nano Lett. 10 (2010) 1082.
[9] S.K. Srivastava, D. Kumar, P.K. Singh, M. Kar, V. Kumar, M. Husain, Excellent antireflection properties of vertical silicon nanowire arrays, Sol. Energy Mater. Sol. Cells 94 (2010) 1506.
[10] K. Peng, S. Lee, Silicon nanowires for photovoltaic solar energy conversion, Adv. Mater. 23 (2011) 198.
[11] X.X. Lin, X. Hua, Z.H. Huang, W.Z. Shen, Realization of high performance silicon nanowire based solar cells with large size, Nanotechnology 24 (2013) 235402.
[12] K. Peng, X. Wang, L. Li, Y. Hu, S. Lee, Silicon nanowires for advanced energy conversion and storage, Nano Today 8 (2013) 75.
[13] S.H. Zhong, Z.G. Huang, X.X. Lin, Y. Zeng, Y.C. Ma, W.Z. Shen, High-efficiency nanostructured silicon solar cells on a large scale realized through the suppression of recombination channels, Adv. Mater. 27 (2015) 555.
[14] J.H. Oh, H.C. Yuan, H.M. Branz, An 18.2%-efficient black-silicon solar cell achieved through control of carrier recombination in nanostructures, Nat. Nanotechnol. 7 (2012) 743.
[15] Z.G. Huang, X.X. Lin, Y. Zeng, S.H. Zhong, X.M. Song, C. Liu, X. Yuan, W.Z. Shen, One-step-MACE nano/microstructures for high-efficient large-size multicrystalline Si solar cells, Sol. Energy Mater. Sol. Cells 143 (2015) 302.
[16] X. Ye, S. Zou, K. Chen, J. Li, J. Huang, F. Cao, X. Wang, L. Zhang, X. Wang, M. Shen, X. Su, 18.45%-efficient multi-crystalline silicon solar cells with novel nanoscale pseudo-pyramid texture, Adv. Funct. Mater. 24 (2014) 6708.
[17] F. Hu, Y. Sun, J. Zha, K. Chen, S. Zou, L. Fang, X. Su, Pre-texturing multi-crystalline silicon wafer via a two-step alkali etching method to achieve efficient nanostructured solar cells, Sol. Energy Mater. Sol. Cells 159 (2017) 121.
[18] Y.F. Zhuang, S.H. Zhong, Z.G. Huang, W.Z. Shen, Versatile strategies for improving the performance of diamond wire sawn mc-Si solar cells, Sol. Energy Mater. Sol. Cells 153 (2016) 18.
[19] Z. Holman, M. Filipic, B. Lipovsek, S. Wolf, F. Smolr, M. Topic, C. Ballif, Parasitic absorption in the rear reflector of a silicon solar cell: simulation and measurement of the sub-bandgap reflectance for common dielectric/metal reflectors, Sol. Energy Mater. Sol. Cells 120 (2014) 426.
[20] T. Dullweber, S. Gatz, H. Hannebauer, T. Falcon, R. Hesse, J. Schmidt, R. Brendel, Towards 20% efficient large-area screen-printed rear-passivated silicon solar cells, Prog. Photovolt. Res. Appl. 20 (2012) 630.
[21] Z.G. Huang, X.M. Song, S.H. Zhong, H.Y. Xu, W.D. Luo, X.D. Zhu, W.Z. Shen, 20.0% efficiency Si nano/microstructures based solar cells with excellent broadband spectral response, Adv. Funct. Mater. 26 (2016) 1892.
[22] F. Ye, W. Deng, W. Guo, R. Liu, D. Chen, Y. Yang, N. Yuan, J. Ding, Z. Feng, P. Altermatt, P. Verlinden, 22.13% efficient industrial p-type mono PERC solar cell, in: Proceedings 43rd IEEE Photovoltaic Spec. Conference, 2016.
[23] Z.P. Huang, N. Geyer, P. Werner, J.D. Boor, U. Gösele, Metal-assisted chemical etching of silicon: a review, Adv. Mater. 23 (2011) 285.
[24] S.Y. Li, W.H. Ma, Y. Zhou, X.H. Chen, Y.Y. Xiao, M.Y. Ma, F. Wei, X. Yang, Fabrication of p-type porous silicon nanowire with oxidized silicon substrate

through one-step MACE, J. Solid State Chem. 213 (2014) 242.

[25] C. Chartier, S. Bastide, C. Lévy-Clément, Metal-assisted chemical etching of silicon in HF-$H_2O_2$, Electrochim. Acta 53 (2008) 5509.

[26] R. Einhaus, E. Vazsonyi, J. Szlufcik, J. Nijs, R. Merten, Isotropic texturing of multicrystalline silicon wafers with acidic texturing solutions, in: Proceedings 26th IEEE Photovoltaic Spec. Conference, 1997.

[27] Z. Holman, S. Wolf, C. Ballif, Improving metal reflectors by suppressing surface plasmon polaritons: a priori calculation of the internal reflectance of a solar cell, Light- Sci. Appl. 2 (2013) e106.

[28] A. Sproul, Dimensionless solution of the equation describing the effect of surface recombination on carrier decay in semiconductors, J. Appl. Phys. 76 (1994) 2851.

[29] A. Richter, S. Glunz, F. Werner, J. Schmidt, A. Cuevas, Improved quantitative description of Auger recombination in crystalline silicon, Phys. Rev. B 86 (2012) 165202.